# Ferroelectricity and negative piezoelectric coefficient in orthorhombic phase pure ZrO$_2$ thin films

José P.B. Silva [a,b,1,*], Marian C. Istrate [c,d,1], Markus Hellenbrand [e], Atif Jan [e], Maximilian T. Becker [e], Joanna Symonowicz [e], Fábio G. Figueiras [f], Veniero Lenzi [a,b], Megan O. Hill [e], Corneliu Ghica [d], Konstantin N. Romanyuk [g,h], Maria J.M. Gomes [a,b], Giuliana Di Martino [e], Luís Marques [a,b], Judith L. MacManus-Driscoll [e,**]

[a] Physics Center of Minho and Porto Universities (CF-UM-UP), University of Minho, Campus de Gualtar, Braga 4710-057, Portugal
[b] Laboratory of Physics for Materials and Emergent Technologies, LapMET, University of Minho, Braga 4710-057, Portugal
[c] Faculty of Physics, University of Bucharest, Atomistilor 405, Ilfov, Magurele 077125, Romania
[d] National Institute of Materials Physics, 105 bis Atomistilor, Magurele 077125, Romania
[e] Department of Materials Science and Metallurgy, 27 Charles Babbage Rd., Cambridge CB3 OFS, UK
[f] IFIMUP & Department of Physics and Astronomy, Sciences Faculty, University of Porto, Rua do Campo Alegre, 687, Porto 4169-007, Portugal
[g] Department of Physics & CICECO-Aveiro Institute of Materials, University of Aveiro, Aveiro 3810-193, Portugal
[h] School of Natural Sciences and Mathematics, Ural Federal University, Ekaterinburg 620026, Russia

## ARTICLE INFO

## ABSTRACT

A new approach for epitaxial stabilisation of ferroelectric orthorhombic (o-) ZrO$_2$ films with negative piezo-electric coefficient in ∼ 8nm thick films grown by ion-beam sputtering is demonstrated. Films on (011)-Nb: SrTiO$_3$ gave the oriented o-phase, as confirmed by transmission electron microscopy and electron backscatter diffraction mapping, grazing incidence x-ray diffraction and Raman spectroscopy. Scanning probe microscopy techniques and macroscopic polarization-electric field hysteresis loops show ferroelectric behavior, with saturation polarization of ∼14.3 μC/cm$^2$, remnant polarization of ∼9.3 μC/cm$^2$ and coercive field ∼1.2 MV/cm. In contrast to the o-films grown on (011)-Nb:SrTiO$_3$, films grown on (001)-Nb:SrTiO$_3$ showed mixed monoclinic (m-) and o-phases causing an inferior remnant polarization of ∼4.8 μC/cm$^2$, over 50% lower than the one observed for the film grown on (011)-Nb:SrTiO$_3$. Density functional theory (DFT) calculations of the SrTiO$_3$/ZrO$_2$ interfaces support the experimental findings of a stable polar o-phase for growth on (011) Nb:SrTiO$_3$, and they also explain the negative piezoelectric coefficient.

## 1. Introduction

The discovery of ferroelectricity in polycrystalline silicon-doped hafnium oxide (Si:HfO$_2$) thin films in 2011 [1,2] offered strong promise for the integration and scalability of ferroelectric films into a range of electronic devices. Since then, a sustained effort has been made to understand the ferroelectric behaviour. This has included exploring other dopants to induce ferroelectricity in HfO$_2$ [3–7], the most investigated dopant being Zr, giving (Hf$_x$Zr$_{1-x}$)O$_2$ (HZO) [8–13].

Extensive research work has been done to integrate polycrystalline HZO materials into ferroelectric memory, ferroelectric field-effect transistors (Fe-FETs), energy storage capacitors, energy harvesters and pyroelectric sensors [14–19]. HZO is appealing because of its a simple pseudo-binary phase, it has a wide bandgap (≈5.3–5.7 eV) [20], and it is compatible with complementary metal oxide semiconductor (CMOS) technologies [14] as it can be processed at ∼400 °C on Si [15].

Much research has been done on polycrystalline HZO, in terms of understanding influences of doping, composition, and strain on the crystal structures and the ferroelectric behaviour [2,9,21–27]. There are three key challenges for polycrystalline HZO: eliminating wake-up, improving retention and reducing fatigue which all cause serious challenges for reliable device operation. The optimum crystal structure for

strong ferroelectric performance in polycrystalline HZO was found to be the *o*-phase [27].

In recent years, the research on ferroelectric HZO was extended to study also the growth and properties of *epitaxial* thin films. Here, the impact of the SrTiO$_3$ (STO) substrate orientation on the ferroelectric performance of the HZO films grown on LSMO/STO substrates were investigated [28,29]. 6.5 nm thick HZO films in HZO/LSMO/STO (110) heterostructures show a maximum $P_r$ of 33 μC/cm$^2$ [28]. These films exhibit a 50% $P_r$ increase for equivalent films on STO(001), owing to the larger *o*-phase content. Moreover, a wake-up effect was not observed due to their epitaxial nature [28].

Recently, 10 nm thick 5% YO$_{1.5}$-doped epitaxial HfO$_2$ films were grown on LSMO/STO (001) or (110) substrates with a *o*-structure with a small rhombohedral distortion [30]. A higher $P_s$ of about 50 μC/cm$^2$ and $P_r$ of about 37 μC/cm$^2$ was achieved for the pure *o*-phase films grown on LSMO/STO (110) substrates due to the high degree of structural order. These films grown on LSMO/STO (110) substrates exhibit a ~12% higher $P_r$ than the ones reported in 6.5 nm thick HZO films grown in LSMO/STO(110) substrates [28]. Moreover, a wake-up free ferroelectric memristor based on epitaxial Y-doped HfO2 films has been recently demonstrated [31].

Following on from the numerous works on HfO$_2$ and doped HfO$_2$, pure films of ZrO$_2$ [11,12] have also been found to be ferroelectric, although there has been less focus on this material, to date. For instance, Bohan et al. have shown ferroelectric behaviour in polycrystalline 45 nm thick ZrO$_2$ films prepared by atomic layer deposition on TiN electrodes [32]. However, very recently, ferroelectricity was observed in ultrathin polycrystalline ZrO$_2$ films grown on Si with a thickness of only 5 Å [33]. The polar o- Pca2$_1$ crystallographic phase has been suggested to be the origin for the existence of the ferroelectricity [12,33–35]. As far as known, there are no reports on the ferroelectric properties of pure *o*-phase ZrO$_2$ films. First-principles calculations support the experimental findings that the Pca2$_1$ *o*-phase of ZrO$_2$ is ferroelectric with a large remnant polarisation (P$_r$) value [36]. We note that other experiments indicate that the rhombohedral R3m phase is ferroelectric [37].

More work needs to be done to investigate the origins of ferroelectricity in ZrO$_2$. It is worthwhile from both a fundamental viewpoint and also a practical one, since ZrO$_2$ is more abundant and accessible than HfO$_2$ [38], exhibits high dielectric constant [39] and it is also CMOS integration compatible. Furthermore, such work may also aid in overcoming the aforementioned challenges in the related HZO material.

In the present work, in epitaxial ZrO$_2$ films, we explore the substrate orientation effect on phase formation and orientation and determine the influence of these parameter on the ferroelectric properties. We reveal that ZrO$_2$ films can be grown epitaxially directly on Nb:STO (011) single crystal substrates as an *o*-phase via domain matching epitaxial growth. Polarization-electric field (P-E) hysteresis loops display a saturation ferroelectric polarization ($P_s$) of ~14 μC/cm$^2$, and an average coercive field ($E_c$) of ~1.2 MV/cm, while piezoresponse force microscopy (PFM) studies show that the films are polar and have a negative piezoelectric coefficient. Due to the epitaxially nature of the films no wake-up effect was observed. Using broad materials characterisation tools as well as density functional theory (DFT) calculations, the existence and stability of the *o*-phase is confirmed. DFT also confirms our experimental evidence of negative piezoelectric effect. Our results give much promise for epitaxial ZrO$_2$ films for electronic applications in future.

## 2. Experimental methods

8-nm thick ZrO$_2$ thin films were grown by ion-beam sputter deposition (IBSD) onto 0.7 wt% Nb-doped SrTiO$_3$ substrates with (001) and (011) orientations. The vacuum chamber was first evacuated down to a low pressure of $1 \times 10^{-6}$ mbar prior to the deposition. During the deposition, the substrate was kept at a temperature of 330 °C at a distance of 87.3 mm from the target. The gas pressure inside the chamber was maintained constant at $2.5 \times 10^{-4}$ mbar. A gas flow of 6.0 ml/min

of Ar and 2.0 ml/min of O$_2$ was introduced into the ion beam gun and the atoms were ionized in the ion source with an RF-power of 120 W. The ion beam was further accelerated at 900 V and the ion beam current was maintained at 31 mA. After the deposition, the thin films were rapid thermally annealed in N$_2$ (6 mbar) at 700 °C, for 60 s.

DFT calculations were performed using the VASP code [40,41], which implements the projector augmented wave method [42]. The generalized gradient approximation (GGA) approximation was used, with the PBESol functional.[43] The plane wave energy cut-off has been set to 600 eV for all calculations. For bulk phase calculations, a $6 \times 6 \times 6$ Gamma-centered k-point grid has been used, while for the interface a $4 \times 2 \times 1$ grid has been used. Interface calculations have been performed under periodic boundary conditions considering ABV (slab) structures, with A, B and V denoting STO, ZrO$_2$, and vacuum respectively, and with the interface normal oriented along the c axis. The thickness of the vacuum slab was set to 20 Å to avoid spurious interactions between periodic images. Dipole moment corrections have been applied in all slab calculations. The lattice constants a and b have been fixed to those of STO and were not relaxed. A total of 8 layers of STO, of which the bottom 2 have been frozen, and 8 layers of ZrO$_2$ were taken into account. The structural relaxation was carried on until atomic forces reached the threshold value of 0.03 eV/Å. The spontaneous polarization of the *o*-ZrO$_2$ was calculated using the modern theory of polarization, as implemented in VASP [44]. The non-polar cubic phase was used as a reference to obtain the polarization of the stress-free unit cell. The in-plane strained unit cells of *o*-phase ZrO$_2$ were built by applying a uniform strain on a and b lattice constants, followed by a relaxation of atomic positions and of the c lattice constant. Atomic forces and the stress component along the c direction were optimized up to 5 meV/Å and 0.1 GPa, respectively. Compared to slab calculations, a tighter atomic force convergence threshold was chosen as polarization and piezoelectric tensor calculations are sensible to small displacements. The piezoelectric tensor component $\varepsilon_{33}$ has been obtained as a function of applied in-plane strain using density functional perturbation theory [45, 46]. To obtain the piezoelectric response component d$_{33}$ of the fully relaxed unit cell of the *o*-phase of ZrO$_2$, we used the formula [47]:

$$d_{33} = \Sigma_{i=1}^{6} e_{3i}\left(C^{-1}\right)_{i3},$$

where the compliance matrix of the fully relaxed unit cell $\mathbf{C^{-1}}$ was calculated by inverting the stiffness matrix, which was obtained using a finite difference method. VESTA software [48] has been used both for generate the graphical representations and to calculate d$_{111}$, through a simulated XRD.

Cross-sectional TEM samples were made by first mechanical thinning followed by Ar$^+$ ion milling on a Gatan PIPS machine at 4 kV acceleration voltage and 6 degrees beam incidence angle. TEM observations were performed using a probe-corrected analytical high-resolution JEMARM 200F electron microscope operated at 200 kV.

Grazing incidence x-ray diffraction (GIXRD) was measured with a High Resolution Panalytical Empyrean vertical diffractometer with an incident angle of 0.5 °, a 1/32 ° incident divergence slit, and a receiving slit opening of 1 mm. The integration time was 20 s per step.

Raman spectroscopy was performed using a single-longitudinal-mode 633 nm laser from Integrated Optics. The power on the sample was 1.5 μW. The Raman signal was collected through optics purchased from Thorlabs into a Andor Shamrock 303i spectrometer with SR-303 shutter coupled to a Newton EMCCD camera from Oxford Instruments.

Electron backscatter diffraction (EBSD) mapping of the ZrO$_2$/(011) Nb:STO sample confirmed the presence of high crystalline quality *o*-phase ZrO$_2$ in the film grown on (011)Nb:STO. EBSD was performed using a ZEISS GeminiSEM 300, with a 60 μm aperture, 15 keV beam current, and 70° tilt with respect to the substrate [011] direction. Electron backscatter patterns (EBSP) were collected on an Oxford Instruments EBSD detector and indexed using the Oxford Aztec software.

Piezo-response force microscopy was done using a scanning probe

microscope INTEGRA Aura (NT-MDT, Russia) equipped with external lock-in amplifier (HFLI, Zurich instruments, Switzerland). Commercial Budget Sensors Tap190E-G probes were used with Cr/Pt coated tips of radius of 25 nm, resonance frequency ~151 kHz and spring constant k about 48 N/m. All piezo-response force microscopy and spectroscopy studies were done out-of-resonance at 21.1(1) kHz in order to decrease electrostatic responses and topographic crosstalk [49]. The images are edited via WSxM 5.0-10.0 software.

For the ferroelectric characterization, circular Au electrodes, with 1 mm diameter, were deposited by thermal evaporation on the upper surface of the films. The ferroelectric hysteresis loops (P-E) were measured at room temperature with a modified Sawyer-Tower circuit [50] using a sinusoidal signal at 1 kHz. Dynamic hysteresis currents were measured by replacing the reference capacitor with a resistor in the Sawyer-Tower circuit. Endurance was measured at room temperature by cycling the sample at a frequency of 100 kHz and measuring polarization loops at 1 kHz.

## 3. Results and discussion

We first present the ferroelectric data of two different films, i.e. $ZrO_2$ films on (001)Nb:STO and on (110)Nb:STO. We then show the structural characteristics and the theoretical calculations, which support the structural and ferro/piezoelectric properties.

### 3.1. Ferroelectric and piezoelectric properties

Fig. 1(a) and (b) displays the room temperature polarization-electric field (P–E) hysteresis loops of the $Au/ZrO_2/Nb:STO$ film capacitors for the (001) and (011) substrate orientations.

The asymmetric shape of the hysteresis loops observed for the films on the two different substrates is due to the difference in work functions between the bottom (Nb:STO) and top (Au) electrodes.

The average values of $P_s$, $P_r$ and $E_c$ are, respectively:
$Au/ZrO_2/(011)Nb:STO$: 14.3 $\mu C/cm^2$, 9.3 $\mu C/cm^2$ and 1.2 MV/cm.
$Au/ZrO_2/(001)Nb:STO$: 17.7 $\mu C/cm^2$, 4.8 $\mu C/cm^2$ and 1.0 MV/cm.

Hence, the highest values of $P_r$ and $E_c$ are observed in the $Au/ZrO_2/(011)Nb:STO$ film capacitor, while a higher $P_s$ value is obtained in the case of the $Au/ZrO_2/(001)Nb:STO$ film capacitor. Moreover, dynamic hysteresis currents were recorded for the $Au/ZrO_2/(011)Nb:STO$ film capacitor (Fig. S1(a)) confirming the ferroelectric nature of the film and also the $E_c$ value was extracted from the P-E loops. The endurance was also investigated for the $Au/ZrO_2/(011)Nb:STO$ film capacitor (Fig. S1(b)). No wake-up effect was observed. However, a slight degradation of 3.0 $\mu C/cm^2$ was observed after $10^6$ cycles.

$P_r$ is an important parameter for non-volatile memory applications and therefore, to learn more about the ferroelectric switching at the nanoscale. The structural properties of the films are discussed in section 2.2. The ferroelectric response of the $ZrO_2/(011)Nb:STO$ films were further investigated by PFM measurements. The topographic scans (Fig. 1(c)) reveal a root mean square roughness near 0.1 nm, i.e. a value
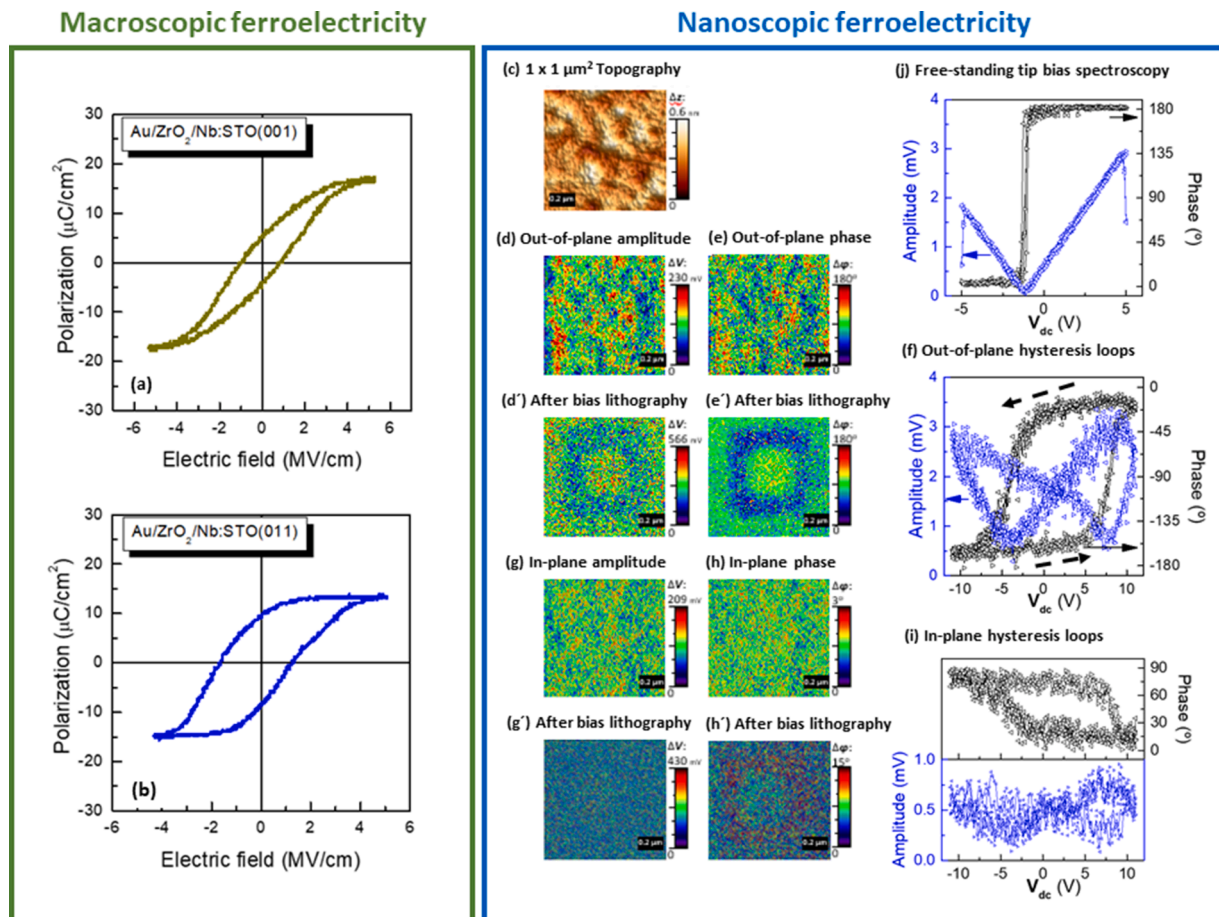


**Fig. 1.** Polarization–Electric field hysteresis loops of the $Au/ZrO_2/Nb:STO$ film capacitors with (a) (001) and (b) (011) Nb:STO substrate orientations. PFM surface scans of the $ZrO_2/(011)Nb:STO$ films. (c) $1 \times 1$ $\mu m^2$ topography images with respective out-of-plane piezo-response in (d), (d') amplitude and (e), (e') phase signals before and after bias lithography stimulation performed at + and -12 $V_{dc}$, and (f) typical hysteresis loops obtained from bias spectroscopy. The arrows show the anti-clockwise rotation of the PFM phase loop. (g), (g'), (h), (h') Corresponding amplitude, phase and (i) loops of lateral-force scans (j) Free-standing tip bias spectroscopy feedback curve.

that is only a fraction of the cell lattice dimensions, thus attesting to the high quality and homogeneity of the $ZrO_2$ layer adhesion to the substrate. From the respective piezo-response out-of-plane amplitude (Fig. 1(d)) and phase (Fig. 1(e)) scans, it was possible to observe very similar spatial distributions of the contrast between very small regions, below 0.5 μm size, without any visible cross-talk to topographic features or associated electrostatic effects. The apparent domains with opposing orientations (shown by blue and red colors) on the as-grown films do not appear to contact directly with each other and exhibit diffuse contours with neutral (green) piezo-response phase. By applying 12 $V_{dc}$ it becomes possible to obtain clear imprints and rewriting of ferroelectric domains (Fig. 1(d') and (e')) as well as reproducible hysteresis switching (Fig. 1(f)) without any topographic alteration.

In Fig. 1(f), butterfly-shaped amplitude loops with ≈180° phase reversing are observed, typical of a ferroelectric-like response. Also, the phase cycles in the same figure reveal a nominal reversal field over 5 V and no substantial decay from saturation to remanence. Interestingly, the phase signal is in-phase (anti-phase) with the ac modulation field at the far negative (positive) dc bias, corresponding to the upwards (downwards) orientation of the polarization. This results in an anti-clockwise rotation of the PFM phase loop (Fig. 1(f)). This behavior is indicative of a negative sign of the piezoelectric stress constant ($\varepsilon_{33}$) in the $ZrO_2$ film. The $d_{33}$ is estimated, using the procedure reported by Dutta et al. [51] with a PFM3 $LiNbO_3$ standard sample, and was found to be between -3 pm/V and -5 pm/V. A similar behavior has also been found in $La:HfO_2$ films [51].

Lateral-force amplitude (Fig. 1(g)) and phase (Fig. 1(h)) scans also detected significant contrast between different regions, indicating that
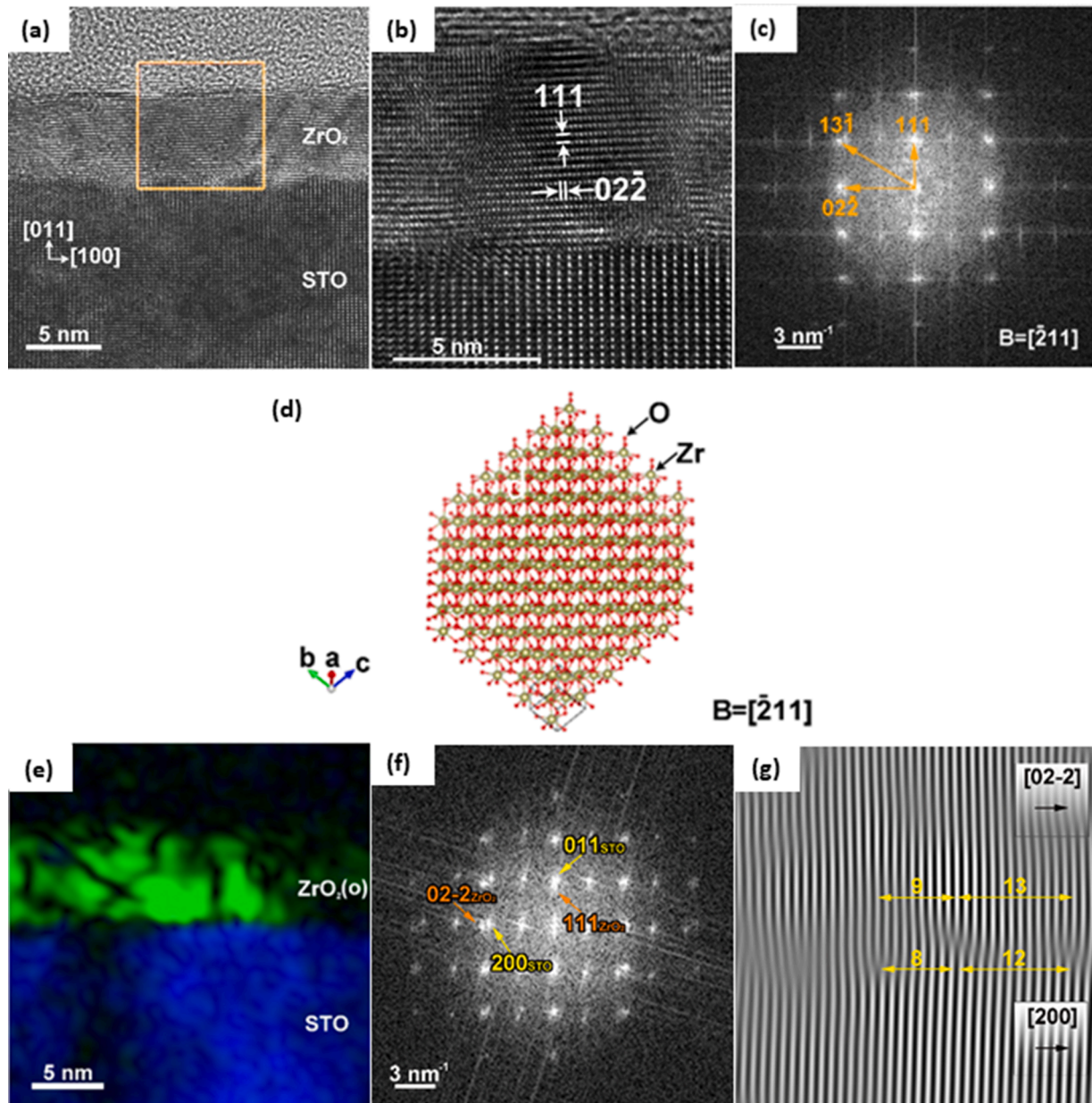


**Fig. 2.** (a) HRTEM image of the $ZrO_2/(011)Nb:STO$ structure; (b) magnified view of an oriented $ZrO_2$ crystallite; (c) FFT pattern corresponding to the area delimited by the orange square in the HRTEM image (a); (d) atomic structural model of $ZrO_2$ along the [-211] direction, in perfect agreement with the structural data provided by the HRTEM micrograph in (b); (e) Bragg Filtered Image obtained using the (111) spot from the FFT diagram; (f) FFT pattern of the micrograph in (b); (g) Fourier filtered micrograph in (b) obtained with the $(02-2)_{ZrO2}$ and $(200)_{STO}$ spots in the FFT diagram (f); the numbers indicate the number of planes in the film (9, 13) continued into the substrate (8, 12) between the cores of successive mismatch dislocations (endings of the supplementary half-planes in $ZrO_2$) showing domains of epitaxial growth with a variable lateral size.

the domains can have some polarization components in-plane. In addition, the small response in the phase imprint (Fig. 1(h')) and clear voltage spectroscopy hysteresis loops (Fig. 1(i)) suggest that a polarization component is switched and retained under an in-plane direction even with poling imposed from an out-of-plane electric field. The existence of horizontal polarization was already demonstrated in *o*-phase La: HfO$_2$ films [52]. Control voltage spectroscopy tests were performed with the tip free-standing from the sample surface (Fig. 1(j)). Feedback measurements were induced only by the attraction/repulsion of the tip near the vertical (few nm distance) region between the free standing tip and the film surface, which produces electrostatic charge build-up. The graph confirms that no spurious contributions were present to delay the switching. Hence, no effects of local retention of charge injection/depletion, nor vacancy migration, nor other electrochemical phenomena could be detected at the film surface during the PFM experiments. This resulted in a proper piezoelectric response (Fig. 1(f)) with the hysteresis loops being consistent with ferroelectric behavior in the *o*-ZrO$_2$ film. Therefore, the piezo-response scans (Fig. 1(g, i)) and the bias spectroscopy loops scans (Fig. 1(j)) can be directly correlated with the ferroelectric properties associated with the *o*-ZrO$_2$ film.

### 3.2. Structural properties

We first investigated the ZrO$_2$/(011)Nb:STO film which showed the most interesting ferroelectric properties of the two substrate orientations, namely nearly 3 x higher $P_r$ as well as a negative piezoelectric coefficient. The cross-section HRTEM images of the ZrO$_2$/(011)Nb:STO film are presented in Fig. 2(a) and enlarged in Fig. 2(b). Both images show an 8-nm thick ZrO$_2$ layer with a sharp substrate-film interface.

In order to analyse the crystalline structure of the film, given the unfavourably large geometrical difference between the film thickness (8 nm) and the projected diameter of the smallest available selecting aperture, we processed Fast Fourier Transform (FFT) patterns of the HRTEM images rather than acquiring selected-area electron diffraction (SAED) patterns. In evaluating the crystalline structure of the ZrO$_2$ film, we considered the similarity between the bulk crystal structures of ZrO$_2$ and HfO$_2$, which are both *m*-phase at room temperature and transform to tetragonal (*t*-phase) between 1050–1200 °C and 1600–1650 °C, respectively. In the case of HfO$_2$, the recently discovered *o*-phase, which has been shown to be responsible for the ferroelectric behavior, can be reliably discerned from the *m*-phase by analysing the (111) diffraction peaks: the (111)$_o$ peak corresponds to an interplanar distance of 0.296 nm between the equivalent {111} planes, while in the case of the *m*-phase the 111$_m$ peak splits in two, corresponding to the {111}$_m$ and {11-1}$_m$ families of planes, spaced at 0.282 nm and 0.314 nm, respectively.

We investigated the (111) diffraction peak as discussed above for analysing the FFT peaks assigned to the ZrO$_2$ layers grown on the (011) Nb:STO substrates. The FFT pattern shown in Fig. 2(c) corresponds to an area delimited by the orange square inside the ZrO$_2$ layer in Fig. 2(a). It contains a well-defined pattern of spots, proving a high crystalline quality of the ZrO$_2$ film in terms of grain size and preferential crystallographic orientation. The main FFT peaks were measured, indexed and assigned to the (13$\bar{1}$), (111) and (02$\bar{2}$) planes of the *o*-structure of ZrO$_2$ in the [$\bar{2}$11] zone axis orientation. The atomic structural model of *o*-ZrO$_2$ in the [$\bar{2}$11] orientation obtained with the VESTA software is provided in Fig. 2(d) in perfect agreement with the experimental data provided by HRTEM. The interplanar distances have been measured also directly on the HRTEM micrograph in Fig. 2(b) where the (111) and (02$\bar{2}$) planes of the *o*-phase have been marked, indicating a *preferential growth orientation of the ZrO$_2$ o-phase with respect to the (011)$_{STO}$ substrate.* To visually emphasize the preferential orientation (111)$_{ZrO2}$ || (011)$_{STO}$ with respect to the substrate, we performed FFT filtering of the HRTEM micrograph. The mixed-color image in Fig. 2(e) has been obtained by filtering out all the FFT intensities, except for the *o*-(111)$_{ZrO2}$ and the (100)$_{STO}$ peaks. The intensity map corresponding to the *o*-(111)$_{ZrO2}$ peak has been

colored in green, while the blue area is generated by FFT filtering using the (100)$_{STO}$ peak. This representation clearly shows that the *o*-ZrO$_2$ phase is present in all the analyzed area, and that it has the (111) orientation. We emphasize that, as far as known, the orientation of ZrO$_2$ films on (011)Nb:STO was not reported previously.

To better describe the film-substrate orientation relationship we have analysed the FFT pattern from a selected area across the interface, including both the thin film and the substrate (Fig. 2(f)). The following film-substrate orientation relationship can be derived: [-211]$_{ZrO2}$ || [01-1]$_{STO}$, (111)$_{ZrO2}$ || (011)$_{STO}$ and (01-1)$_{ZrO2}$ || (100)$_{STO}$. The same preferential orientation with respect to the substrate can be noticed at the neighboring grains. However, despite the good matching between the (02-2)$_{ZrO2}$ planes (d$_{02-2}$=0.186 nm) in the film and the (200)$_{STO}$ planes (d$_{200}$=0.194 nm) in the substrate leading to a lattice mismatch of 4%, the situation is different along the perpendicular in-plane direction where the mismatch between the (-211)$_{ZrO2}$ planes (d$_{-211}$=0.211 nm) in the film and the (01-1)$_{STO}$ planes (d$_{01-1}$=0.275 nm) in the substrate measures 30%. Given the high value of the film-substrate lattice mismatch, the observed orientation relationship cannot be explained as a result of conventional epitaxial growth base on linear elasticity theory. This epitaxial relationship for heterointerfaces in highly mismatched systems can be instead explained via a near coincidence lattice model [53] or domain matching epitaxy (DME), with the formation of geometrical misfit dislocations or of coincidence units with variable lateral sizes to accommodate the coincidence lattice misfit [54]. The image in Fig. 2(g) represents the Fourier filtered micrograph in (b) obtained with the (02-2)$_{ZrO2}$ and (200)$_{STO}$ spots in the FFT diagram (f). The filtered image shows the formation of misfit dislocations at the ZrO$_2$-STO interface delimiting domains of epitaxial growth with a variable lateral size. Similar heteroepitaxial relationships in systems with a large lattice misfit have been recently evidenced for Hf$_{0.5}$Zr$_{0.5}$O$_2$ thin films grown on La$_{2/3}$Sr$_{1/3}$MnO$_3$/STO(001) substrates [55] and Hf$_{0.5}$Zr$_{0.5}$O$_2$ films on La$_{2/3}$Sr$_{1/3}$MnO$_3$/SrTiO$_3$(110) substrates [28]. To the best of our knowledge, this is the first experimental evidence that pure *o*-phase ZrO$_2$ films can be grown through DME mechanism directly on Nb:STO substrates.

In the case of the ZrO$_2$ layers grown on the (001)Nb:STO, an *o* + *m* phase mixture occurs. Detailed analysis is given in SI (Fig. S2). Overall, the HRTEM investigations indicate that the substrate orientation plays a decisive role in controlling both the type and orientation of the as-grown ZrO$_2$ phases.

Coming back now to the observed average values of $P_s$, $P_r$ and $E_c$, the coexistence of phases in the ZrO$_2$ films grown on the Nb:STO(001) will reduce domain pinning propagation [56] and therefore lead to an increase of the $P_s$ value. Moreover, the observed elongation of the P-E loop observed in the Au/ZrO$_2$/(001)Nb:STO film capacitor is due to the formation of polar nanograins/domains, as observed in perovskite systems [57]. In addition, the higher $E_c$ observed in the case of Au/ZrO$_2$/(011) Nb:STO film capacitor is due to the epitaxial growth of the ZrO$_2$ layer. As observed in *o*-HfO$_2$, epitaxial films exhibit higher $E_c$ [58], and it was recently reported that the larger $E_c$ is caused by the clamping of the epitaxial layer [59].

In order to confirm the long-range order of the crystalline *o*-phase ZrO$_2$ film grown on (011)-oriented Nb:STO, GIXRD measurements were carried out. A representative result of such a scan is presented in Fig. 3 (a) and clearly demonstrates the presence of a diffraction peak centered at 2θ ≈ 29.6 ° (d111 = 3.02 Å). Based on established crystallographic databases [60], this peak position fits very well with the confirmed position of (111) *o*-ZrO$_2$. While the (101) peak for tetragonal ZrO$_2$ is in proximity ($\gtrsim$ 30 °) of the measured peak, the TEM results discussed above support the identification of the measured peak as (111) *o*-ZrO$_2$. For the ZrO$_2$/(001)Nb:STO sample, the GIXRD pattern did not reveal any peak at this position (shown in Fig. S3(a) and detailed in SI). To further investigate the crystalline phases in the 8 nm-thick ZrO$_2$ films grown on both the (011)Nb:STO and (001)Nb:STO substrates, Raman spectra were collected. Detailed analysis is given in SI (Fig. S3(b)–(d)).
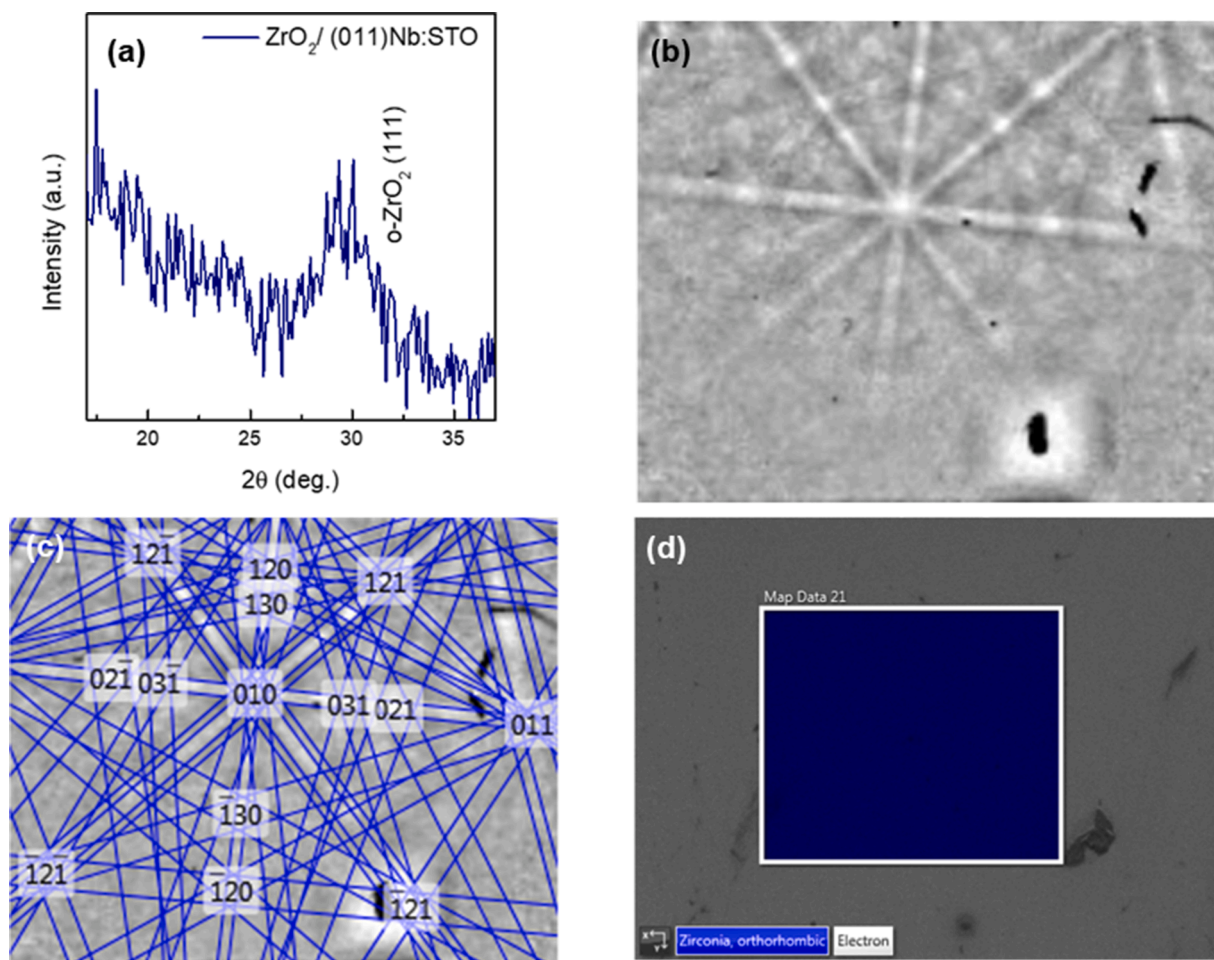
**Fig. 3.** GIXRD pattern and EBSP patterns and Electron backscatter diffraction (EBSD) map of $ZrO_2$ film grown on (011)Nb:STO. (a) GIXRD of $ZrO_2$/(011)Nb:STO. (b) Example EBSP for $ZrO_2$ on (011)Nb:STO; all patterns measured show similar Kikuchi lines. (c) The best indexing of the EBSP in (a), indexed to o-$ZrO_2$; (d) Example EBSD map, showing 100% indexing to o-$ZrO_2$ for a ~30 μm$^2$ area; all regions measured showed similar single crystalline behaviour with minimal change in the EBSP across the film.

To further confirm the *o*-phase pure nature of the $ZrO_2$ film grown on /(011)Nb:STO, electron backscatter patterns (EBSP) were collected on multiple regions of the sample spanning approximately 3 mm$^2$. All patterns were comparable to the EBSP in Fig. 3(b), with Kikuchi lines fitting well to the o-$ZrO_2$ phase as seen in Fig. 3(c). Microscale maps were taken at multiple positions on the sample. All maps contained 100% o-$ZrO_2$ phase indexed EBSPs, like the example in Fig. 3(d). Minimal orientation change was identified in the film, supporting the TEM observation of highly textured (111)-oriented $ZrO_2$.

### 3.3. Density functional theory calculations

DFT calculations were performed to verify the stability of the *o*-$ZrO_2$ phase on (011)-oriented Nb:STO from a theoretical perspective. We simplified the system by neglecting the presence of Nb. Moreover, we used a completely defect-free interface in the simulations. The (011)-oriented STO has lattice constants of $a = 3.905$ Å and $b = 5.5225$ Å, while the fully relaxed o-$ZrO_2$ unit cell has $a = 5.047$ Å, $b = 5.253$ Å and $c = 5.067$ Å, and a $d_{111}$ of 2.957 Å, which makes the spontaneous polarization directed along the c direction [61]. Apart from this, the HRTEM results and the fully-relaxed calculations are in almost exact agreement. Based on the experimental results, calculations were performed for the o-(111)$ZrO_2$/STO(011) interface in an ABV structure, with A being the STO substrate, B the o-$ZrO_2$ film and V the vacuum.

The *o*-phase was not found to be stable from STO (011) from DFT calculations. This might be expected as our simulations are in the ultra-thin film limit, and in such cases the (111) texture is not stable, as experimentally shown by Cheema et al. for $Hf_{0.8}Zr_{0.2}O_2$ films [62] i.e. ultrathin $Hf_{0.8}Zr_{0.2}O_2$ films are textured, while 10-nm thick are (111) highly oriented. Moreover, it was further proposed by Nukala et al. that the preferred orientation in ultrathin o-HZO films might be (100), with distortions of oxygen tetrahedra causing the appearance of large $d_{111}$ [63]. For these reasons, the (001) orientation of o-$ZrO_2$ was instead chosen for the o-$ZrO_2$/STO(011) interface calculations. To reduce mismatch between film and substrate, we replicated the substrate and film unit cells along *a,* 4 and 3 times, respectively. The final interface supercell had lattice constants of $a = 15.62$ Å and $b = 5.5225$ Å, with a resulting strain in the o-$ZrO_2$ of 3.1 % along a and 5.1 % along b. As shown in Fig. 4(a), this strained *o*-phase was found to be stable, with minor displacements observed within the very first layers of the $ZrO_2$ film and at the $ZrO_2$/vacuum interfaces. Moreover, the *o*-phase stability was confirmed to be independent of the choice of STO substrate termination at the $ZrO_2$ interface (See Supporting Information). Due to the strain, the calculated c lattice constant is reduced to 4.94 Å, and the calculated $d_{111}$ slightly increased to 3.00 Å, which is close to the value obtained in the GIXRD experiments. The variation of $d_{111}$ with the in-plane strain ($\varepsilon_{IP}$) is represented in Fig. 4(b) and it is possible to observe a linear relationship between $d_{111}$ and $\varepsilon_{IP}$. In the inset of the same figure it is schematically shown how $\varepsilon_{IP}$ changes with $d_{111}$ for the o-$ZrO_2$ unit cell. Given this similarity of parameters and the apparent challenge of simulating ultra-thin films [62], we investigated general trends of polarization and piezoelectric properties of the o-$ZrO_2$ phase in
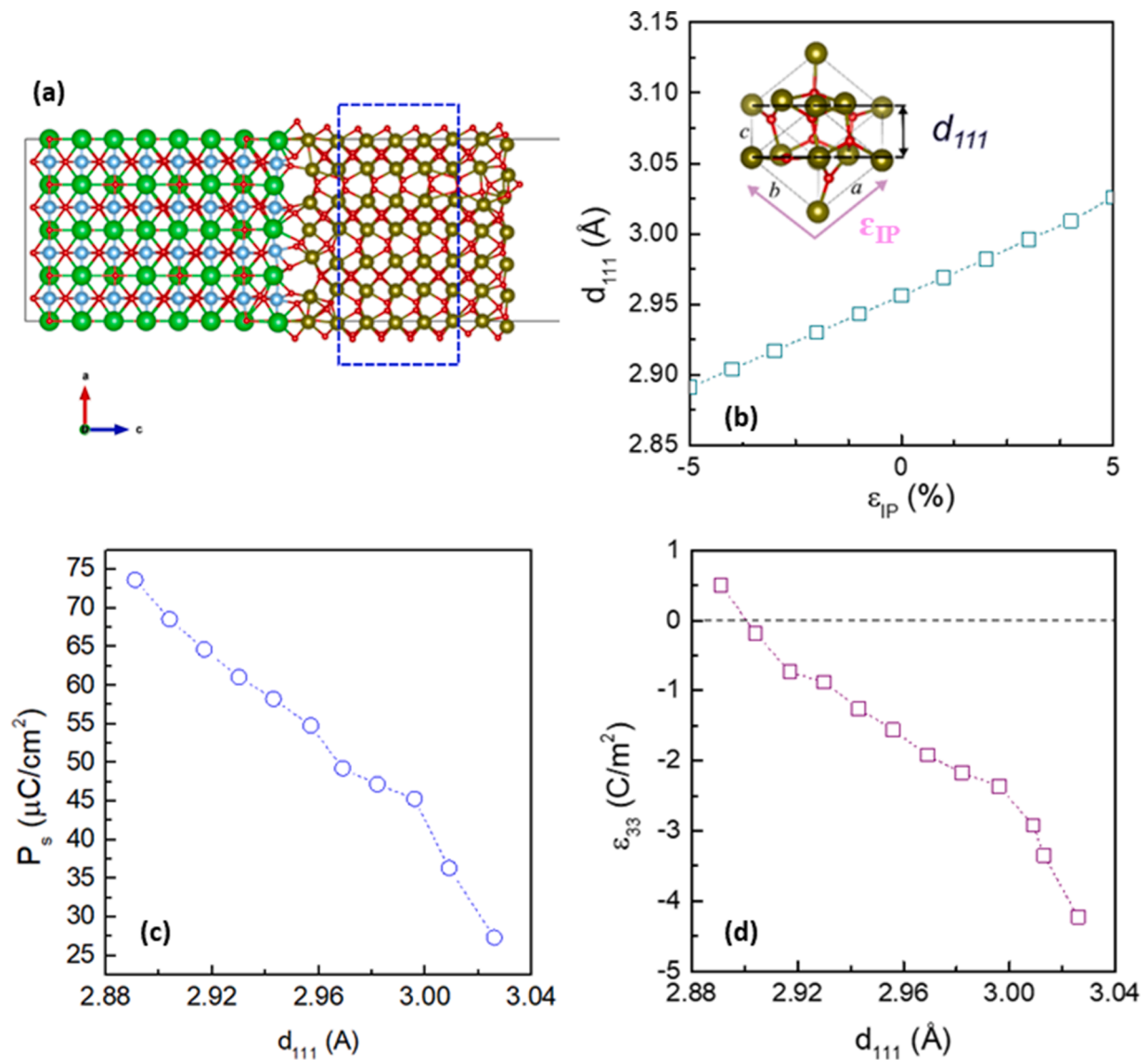
**Fig. 4.** DFT calculations for the (001)ZrO$_2$/(011)Nb:STO films. (a) A schematic crystal structure showing the (011) STO/o-ZrO$_2$(001) interface after relaxation. The dashed box in the ZrO$_2$ film highlights the regions where the o-phase can be clearly recognized by the typical distortion of the oxygen atoms[47]. In this picture Sr is in green, Ti in cyan, Zr in ochre and O in red. (b-d) Calculations of ferroelectric parameters for ZrO$_2$ films undertaken by DFT. (b) Magnitude of the d$_{111}$ as a function of the $\varepsilon_{IP}$. The inset shows schematically how the $\varepsilon_{IP}$ value change the d$_{111}$ value in an o-ZrO$_2$ phase unit cell. (c) Magnitude of P$_s$ along the (001) direction of o-ZrO$_2$, expressed as a function of d$_{111}$ and (d) $\varepsilon_{33}$ component of the piezoelectric response, expressed as a function of d$_{111}$.

this stable system, rather than a quantitative comparison between simulations and experiments.

To understand the effect of substrate-induced strain on the ZrO$_2$ film polarization, the $P_s$ of o-ZrO$_2$ was calculated along the (001) direction as a function of isotropic in-plane strain ranging from -5% to 5%. From Fig. 4(c), it is clear that negative in-plane strain greatly enhances $P_s$, with an increased effect for larger strains. The fully relaxed o-ZrO$_2$ unit cell, which is similar to the one obtained from the TEM results of Fig. 2 (i.e. lattice parameter values of $a = 0.50401$ nm, $b = 0.507445$ nm and $c = 0.526298$ nm), corresponding to a d$_{111}$ of 2.957 Å, gives a $P_s$ value around 54.78 μC/cm$^2$ (Fig. 4(c)). The calculated $P_s$ for the o-phase (111) ZrO$_2$/(011)Nb:STO film obtained from Fig. 4(c), which upon considering the projection along the (111) direction gives a value of 31.62 μC/cm$^2$ is significantly larger than the measured $P_s$ of the film, shown in Fig. 1(b). This difference may be associated with the fact that DFT calculations of polarization assume an ideal bulk-phase of o-ZrO$_2$ and do not consider the specifics of a real thin film. For example, substrate clamping effect, oxygen vacancies, and other defects would produce a

lower $P_s$ value [59].

The anti-clockwise rotation of the PFM phase loop observed (Fig. 1 (f)) suggests the presence of a negative longitudinal piezoelectric constant, as was recently observed in HfO$_2$ [51], where the $c$ lattice constant was found to decrease as the strain increases. To verify our observed negative piezoelectric constant (shown in Figure 1(f)), the total piezoelectric coefficient $\varepsilon_{33}$ of the o-ZrO$_2$ unit cell was calculated as a function of isotropic in-plane strain, ranging from -5% to 5%, as well as for the fully relaxed cell, and the one found in the predicted o-ZrO$_2$/(011)STO interface, and it is reported in Fig. 4(d). It was found that the fully relaxed unit cell, which is similar to the one obtained from the TEM results of Fig. 2, has a d$_{111}$ value of 2.957 Å which gives a $\varepsilon_{33}$ value of -1.56 C/m$^2$ (Fig. 4(d)), corresponding to a *negative* piezoelectric constant $d_{33}$ of -2.67 pm/V. The appearance of a negative piezoelectric coefficient was confirmed by calculating the variation of $P_s$ upon the application of strain of ±1% along the polarisation direction. It was found that $P_s$ decreased to 52.41 μC/cm$^2$ upon applying a tensile strain, and increased to 55.77 μC/cm$^2$ upon applying a compressive strain, in line with what

reported elsewhere [64]. This is confirmed also when the Nb:STO substrate-induced (anisotropic) strain of 3 % along *a* and 5 % along *b* (corresponding to d$_{111}$ of 3.013 Å) is present, which gives a value of $\varepsilon_{33}$ o*f* -3.35 C/m$^2$. Therefore, our DFT calculation results confirm the experimental results, showing the presence of a negative piezoelectric constant in o-ZrO$_2$ films grown on (011)STO substrate. The predicted *d$_{33}$* value was found to be -2.67 pm/V, which is close to the experimental one (between -3 pm/V and -5 pm/V).

Overall, our calculations show that the o-ZrO$_2$/(011)STO interface is stable and that in-plane strain appears to be a key factor in tuning $P_s$ and $\varepsilon_{33}$ of o-ZrO$_2$ films. This is consistent with the theoretical work of Dutta et al. [51] who investigated the piezoelectric properties of o-HfO$_2$ and showed that the longitudinal piezoelectric response ($\varepsilon_{33}$ or d$_{33}$) was reversed by in-plane strain, *without* switching the polarization. Similar to what the authors proposed to o-HfO$_2$, when ZrO$_2$ is strained along its polar axis, the material will react by shifting the oxygen anions responsible for its $P_s$, so as to best preserve the equilibrium distance of the corresponding Zr-O bonds. This atomic rearrangement affects the polarization in such a way that it grows when the strain is compressive, yielding a negative longitudinal piezoelectric coefficient. For large in-plane compressions of 5% in ZrO$_2$, similar to what was observed to o-HfO$_2$ the values found for $\varepsilon_{33}$ become positive. Therefore, the negative sign of d$_{33}$ was attributed to the chemical coordination of the active oxygen atoms that are responsible for the appearance of the polar Pca2$_1$ phase in o-HfO$_2$ [51]. In fact, it was recently predicted that the behaviour in o-ZrO$_2$ is similar to that observed in o-HfO$_2$ [64]. We note that previous to our calculations and experiments, there has been no experimental reports about the possibility of obtaining a negative longitudinal piezoelectric response in ZrO$_2$ films. Therefore, our results confirm that o-ZrO$_2$ has a similar behavior to o-HfO$_2$. Work on the hypothesis that changing the sign of the piezoelectric response of ZrO$_2$ by controlling active oxygen through in-plane strain or doping is now eagerly anticipated.

## 4. Conclusions

In conclusion, we have demonstrated ferroelectricity in epitaxial orthorhombic (o)-(111)-oriented ZrO$_2$ films. The films were 8 nm thick and the (111) orientation was achieved by growing on (011) Nb:STO substrates. The films showed a spontaneous polarization of ~14 μC/cm$^2$, coercive field of ~1.2 MV/cm, and negative piezoelectric coefficient, d$_{33}$. Also, polar domains could be written/read electrically and reversibly switched with a phase change of 180°. DFT calculations confirmed that it is possible to obtain a negative piezoelectric coefficient in ZrO$_2$ thin films. Considering the much greater abundance and high dielectric constant of ZrO$_2$, and the results of this study, there is strong potential for epitaxial ZrO$_2$ thin films for negative capacitance ferroelectrics, e.g. as superior gate dielectrics in CMOS transistors, as well as in next-generation memory and sensing devices.

## Supporting information

Dynamic hysteresis current and endurance properties of the ZrO$_2$/Nb:STO samples, structural properties of the ZrO$_2$/Nb:STO samples and stability of the o-phase of ZrO$_2$ on (011)-oriented STO substrates.

## CRediT authorship contribution statement

**José P.B. Silva:** Formal analysis, Methodology, Supervision, Writing – review & editing, Writing – original draft. **Marian C. Istrate:** Methodology, Writing – review & editing, Writing – original draft. **Markus Hellenbrand:** Methodology, Writing – review & editing, Writing – original draft. **Atif Jan:** Methodology, Writing – review & editing, Writing – original draft. **Maximilian T. Becker:** Methodology, Writing – review & editing, Writing – original draft. **Joanna Symonowicz:** Methodology, Writing – review & editing, Writing – original draft. **Fábio G. Figueiras:** Methodology, Writing – review & editing, Writing – original draft. **Veniero Lenzi:** Methodology, Writing – review & editing, Writing – original draft. **Megan O. Hill:** Methodology, Writing – review & editing, Writing – original draft. **Corneliu Ghica:** Methodology, Writing – review & editing, Writing – original draft. **Konstantin N. Romanyuk:** Methodology, Writing – review & editing, Writing – original draft. **Maria J.M. Gomes:** Supervision, Writing – review & editing, Writing – original draft. **Giuliana Di Martino:** Supervision, Writing – review & editing, Writing – original draft. **Luís Marques:** Methodology, Writing – review & editing, Writing – original draft. **Judith L. Mac-Manus-Driscoll:** Supervision, Writing – review & editing, Writing – original draft.

## Declaration of Competing Interest

The authors declare that they have no known competing financial interests or personal relationships that could have appeared to influence the work reported in this paper.

## Data Availability

Data will be made available on request.

## Acknowledgments

## Supplementary materials

Supplementary material associated with this article can be found, in the online version, at doi:10.1016/j.apmt.2022.101708.

## References

[1] T.S. Boescke, J. Mueller, D. Braeuhaus, U. Schroeder, U. Boettger, Ferroelectricity in hafnium oxide thin films, Appl. Phys. Lett. 99 (2011), 102903.

[2] U. Schroeder, M.H. Park, T. Mikolajick, C.S. Hwang, The fundamentals and applications of ferroelectric $HfO_2$, Nat. Rev. Mater. 7 (2022) 653–669.

[3] S. Mueller, C. Adelmann, A. Singh, S. Van Elshocht, U. Schroeder, T. Mikolajick, Ferroelectricity in Gd-doped $HfO_2$ thin films, ECS J. Solid State Sci. Technol. 1 (2012) N123.

[4] S. Mueller, J. Mueller, A. Singh, S. Riedel, J. Sundqvist, U. Schroeder, T. Mikolajick, Incipient ferroelectricity in Al-doped $HfO_2$ thin films, Adv. Funct. Mater. 22 (2012) 2412.

[5] T. Schenk, S. Mueller, U. Schroeder, R. Materlik, A. Kersch, M. Popovici, C. Adelmann, S. Van Elshocht, T. Mikolajick, Strontium doped hafnium oxide thin films: wide process window for ferroelectric memories, in: Proceedings of the European Solid-State Device Research Conference ESSDERC 2013, 2013, pp. 260–263, https://doi.org/10.1109/ESSDERC.2013.6818868.

[6] T. Shimizu, K. Katayama, T. Kiguchi, A. Akama, T.J. Konno, O. Sakata, H. Funakubo, The demonstration of significant ferroelectricity in epitaxial Y-doped $HfO_2$ film, Sci. Rep. 6 (2016) 32931.

[7] J. Muller, T. Boscke, S. Muller, E. Yurchuk, P. Polakowski, J. Paul, D. Martin, T. Schenk, K. Khullar, A. Kersch, W. Weinreich, S. Riedel, K. Seidel, A. Kumar, T. Arruda, S. Kalinin, T. Schlosser, R. Boschke, R. van Bentum, U. Schroder, T. Mikolajick, Ferroelectric hafnium oxide: A CMOS-compatible and highly scalable approach to future ferroelectric memories, in: Proceedings of the IEEE International Electron Devices Meeting (IEDM), 2013, 10.8.1-10.8.4.

[8] G. Karbasian, A. Tan, A. Yadav, E.M.H. Sorensen, C.R. Serrao, A.I. Khan, K. Chatterjee, S. Kim, C. Hu, S. Salahuddin, Ferroelectricity in $HfO_2$ thin films as a function of Zr doping, in: Proceedings of the International Symposium on VLSI Technology, Systems and Application, International Symposium on VLSI Technology, Systems and Application (VLSI-TSA), 2017, https://doi.org/10.1109/VLSI-TSA.2017.7942488.

[9] J. Müller, T.S. Böscke, U. Schröder, S. Mueller, D. Bräuhaus, U. Böttger, L. Frey, T. Mikolajick, Ferroelectricity in simple binary $ZrO_2$ and $HfO_2$, Nano Lett. 12 (2012) 4318–4323.

[10] J. Bouaziz, P.R. Romeo, N. Baboux, R. Negrea, L. Pintilie, B. Vilquin, Dramatic impact of pressure and annealing temperature on the properties of sputtered ferroelectric HZO layers, APL Mater. 7 (2019), 081109.

[11] S. Starschich, T. Schenk, U. Schroeder, U. Boettger, Ferroelectric and piezoelectric properties of $Hf_{1-x}Zr_xO_2$ and pure $ZrO_2$ films, Appl. Phys. Lett. 110 (2017), 182905.

[12] J.P.B. Silva, J.M.B. Silva, K.C. Sekhar, H. Palneedi, M.C. Istrate, R.F. Negrea, C. Ghica, A. Chahboun, M. Pereira, M.J.M. Gomes, Energy storage performance of ferroelectric $ZrO_2$ film capacitors: effect of $HfO_2:Al_2O_3$ dielectric insert layer, J. Mater. Chem. A 8 (2020) 14171–14177.

[13] M. Hoffmann, F.P.G. Fengler, M. Herzig, T. Mittmann, B. Max, U. Schroeder, R. Negrea, L. Pintilie, S. Slesazeck, T. Mikolajick, Unveiling the double-well energy landscape in a ferroelectric layer, Nature 565 (2019) 464–467.

[14] A. Kashir, S. Oh, H. Hwang, Defect engineering to achieve wake-up free $HfO_2$-based ferroelectrics, Adv. Eng. Mater. 23 (2021), 2000791.

[15] S.J. Kim, J. Mohan, J. Lee, J.S. Lee, A.T. Lucero, C.D. Young, L. Colombo, S. R. Summerfelt, T. San, J. Kim, Effect of film thickness on the ferroelectric and dielectric properties of low-temperature (400 °C) $Hf_{0.5}Zr_{0.5}O_2$ films, Appl. Phys. Lett. 112 (2018), 172902.

[16] W.Y. Liu, J.J. Liao, J. Jiang, Y.C. Zhou, Q. Chen, S.T. Mo, Q. Yang, Q.X. Peng, L. M. Jiang, Highly stable performance of flexible $Hf_{0.6}Zr_{0.4}O_2$ ferroelectric thin films under multi-service conditions, J. Mater. Chem. C 8 (2020) 3878–3886.

[17] Y. Wei, S. Matzen, T. Maroutian, G. Agnus, M. Salverda, P. Nukala, Q. Chen, J. Ye, P. Lecoeur, B. Noheda, Magnetic tunnel junctions based on ferroelectric $Hf_{0.5}Zr_{0.5}O_2$ tunnel barriers, Phys. Rev. Appl. 12 (2019), 031001.

[18] M. Halter, L. Bégon-Lours, V. Bragaglia, M. Sousa, B.J. Offrein, S. Abel, M. Luisier, J. Fompeyrine, Back-End, CMOS-compatible ferroelectric field-effect transistor for synaptic weights, ACS Appl. Mater. Interfaces 12 (2020) 17725–17732.

[19] P.D. Lomenzo, C.C. Chung, C. Zhou, J.L. Jones, T. Nishida, Doped $Hf_{0.5}Zr_{0.5}O_2$ for high efficiency integrated supercapacitors, Appl. Phys. Lett. 2017 (110) (2017), 232904.

[20] S. Chakraborty, M.K. Bera, G.K. Dalapati, D. Paramanik, S. Varma, P.K. Bose, S. Bhattacharya, C.K. Maiti, High dielectric constant $ZrO_2$ films by atomic layer deposition technique on Germanium substrates, Semicond. Sci. Technol. 21 (2006) 467–472.

[21] H. Mulaosmanovic, E.T Breyer, S. Dünkel, S. Beyer, T. Mikolajick, S. Slesazeck, Ferroelectric field-effect transistors based on $HfO_2$: a review, Nanotechnology 32 (2021), 502002.

[22] J. Bouaziz, P.R. Romeo, N. Baboux, B. Vilquin, Huge Reduction of the wake-up effect in ferroelectric HZO thin films, ACS Appl. Electron. Mater. 1 (2019) 1740–1745.

[23] A. Kashir, H. Kim, S. Oh, H. Hwang, Large remnant polarization in a wake-up free $Hf_{0.5}Zr_{0.5}O_2$ ferroelectric film through bulk and interface engineering, ACS Appl. Electron. Mater. 3 (2021) 629–638.

[24] M.H. Park, T. Schenk, C.M. Fancher, E.D. Grimley, C. Zhou, C. Richter, J. M. LeBeau, J.L. Jones, T. Mikolajick, U. Schroeder, A comprehensive study on the structural evolution of $HfO_2$ thin films doped with various dopants, J. Mater. Chem. C 5 (2017) 4677—4690.

[25] M.G. Kozodaev, A.G. Chernikova, E.V. Korostylev, M.H. Park, R.R. Khakimov, C. S. Hwang, A.M. Markeev, Mitigating wakeup effect and improving endurance of ferroelectric $HfO_2$-$ZrO_2$ thin films by careful La-doping, J. Appl. Phys. 125 (2019), 034101.

[26] S. Estandía, N. Dix, J. Gazquez, I. Fina, J. Lyu, M.F. Chisholm, J. Fontcuberta, F. Sánchez, Engineering ferroelectric Hf0.5Zr0.5O2 thin films by epitaxial stress. ACS Appl. Electron. Mater. 1, (201) 1449–1457.

[27] J.P.B. Silva, K.C. Sekhar, R.F. Negrea, J.L. MacManus-Driscoll, L. Pintilie, Progress and perspective on different strategies to achieve wake-up-free ferroelectric hafnia and zirconia-based thin films, Appl. Mat. Tod. 26 (2022), 101394.

[28] T. Song, H. Tan, S. Estandía, J. Gàzquez, M. Gich, N. Dix, I. Fina, F. Sánchez, Improved polarization and endurance in ferroelectric $Hf_{0.5}Zr_{0.5}O_2$ films on $SrTiO_3$(110), Nanoscale 14 (2022) 2337–2343.

[29] P. Jiao, J. Li, Z. Xi, X. Zhang, J. Wang, Y. Yang, Y. Deng, D. Wu, Ferroelectric $Hf_{0.5}Zr_{0.5}O_2$ thin films deposited epitaxially on (110)-oriented $SrTiO_3$, Appl. Phys. Lett. 119 (2021), 252901.

[30] Y. Yun, P. Buragohain, M. Li, Z. Ahmadi, Y. Zhang, X. Li, H. Wang, J. Li, P. Lu, L. Tao, H. Wang, J.E. Shield, E.Y. Tsymbal, A. Gruverman, X. Xu, Intrinsic ferroelectricity in Y-doped $HfO_2$ thin films, Nat. Mater. 21 (2022) 903–909.

[31] M.L. Müller, M.T. Becker, N. Strkalj, J.L. MacManus-Driscoll, Schottky-to-Ohmic switching in ferroelectric memristors based on semiconducting $Hf_{0.93}Y_{0.07}O_2$ thin films, Appl. Phys. Lett. 121 (2022), 093501.

[32] B. Xu, P.D. Lomenzo, A. Kersch, T. Mikolajick, U. Schroeder, Influence of Si-doping on 45 nm thick ferroelectric $ZrO_2$ films (ACS Appl, Electron. Mater. 4 (2022) 3648–3654.

[33] S.S. Cheema, N. Shanker, S.L.H. Rho, C.H. Hsu, V.A. Stoica, Z. Zhang, J. W. Freeland, P. Shafer, C.P. Grigoropoulos, J. Ciston, S. Salahuddin, Emergent ferroelectricity in subnanometer binary oxide films on silicon, Science 376 (2022) 648–652.

[34] C.Y. Wang, C.I. Wang, S.H. Yia, T.J. Chang, C.Y. Chou, Y.T. Yin, M. Shiojiri, M. J. Chen, Paraelectric/antiferroelectric/ferroelectric phase transformation in as-deposited $ZrO_2$ thin films by the TiN capping engineering, Mater. Des. 195 (2020), 109020.

[35] K.W. Huang, S.H. Yia, Y.S. Jiang, W.C. Kao, Y.T. Yin, D. Beck, V. Korolkov, R. Proksch, J. Shieh, M.J. Chen, Sub-7-nm textured ZrO2 with giant ferroelectricity, Acta Mater. 205 (2021), 116536.

[36] S.E. Reyes-Lillo, K.F. Garrity, KM. Rabe, Antiferroelectricity in thin-film ZrO2 from first principles, Phys. Rev. B 90 (14) (2014), 140103.

[37] J.P.B. Silva, R.F. Negrea, M.C. Istrate, S. Dutta, H. Aramberri, J. Íñiguez, F. G. Figueiras, C. Ghica, K.C. Sekhar, A.L. Kholkin, Wake-up free ferroelectric rhombohedral phase in epitaxially strained $ZrO_2$ thin films, ACS Appl. Mater. Interfaces 13 (43) (2021) 51383–51392.

[38] Ed. By J. Drennan, B.C.H. Steele, R.J. Brook, Zirconia and Hafnia in Concise Encyclopedia of Advanced Ceramic Materials, Elsevier Ltd., 1991, https://doi.org/10.1016/C2009-1-28294-3. Ed. By.

[39] G. Antoniou, N.R. Halcovitch, M. Mucientes, W.I. Milne, A. Nathan, J. L. MacManus-Driscoll, O.V. Kolosov, G. Adamopoulos, Solution-processed thin film transistors incorporating YSZ gate dielectrics processed at 400 °C, APL Mater. 10 (2022), 031109.

[40] G. Kresse, J. Hafner, Ab initio molecular dynamics for liquid metals, Phys. Rev. B 47 (1993) 558.

[41] G. Kresse, J. Furthmuller, G. Kresse, J. Furthmuller, Efficiency of ab-initio total energy calculations for metals and semiconductors using a plane-wave basis set, Comput. Mater. Sci. 6 (1996) 15–50.

[42] G. Kresse, D. Joubert, From ultrasoft pseudopotentials to the projector augmented-wave method, Phys. Rev. B 59 (1999) 1758–1775.

[43] J.P. Perdew, A. Ruzsinszky, G.I. Csonka, O.A. Vydrov, G.E. Scuseria, L. A. Constantin, X. Zhou, K. Burke, Restoring the density-gradient expansion for exchange in solids and surfaces, Phys. Rev. Lett 100 (2008), 136406.

[44] R. Resta, Macroscopic polarization in crystalline dielectrics: the geometric phase approach, Rev. Mod. Phys 66 (1994) 899.

[45] M. Gajdoš, K. Hummer, G. Kresse, J. Furthmüller, F. Bechsted, Linear optical properties in the projector-augmented wave methodology, Phyd. Rev. B 73 (2006), 045112.

[46] D.R. Hamann, X. Wu, K.M. Rabe, D. Vanderbilt, Metric tensor formulation of strain in density-functional perturbation theory, Phys. Rev. B 71 (2005), 035117.

[47] F. Bernardini, V. Fiorentini, First-principles calculation of the piezoelectric tensor d↓↓ of III–V nitrides, Appl. Phys. Lett. 80 (2002) 4145.

[48] K. Momma, F. Izumi, VESTA3 for three-dimensional visualization of crystal, volumetric and morphology data, J. Appl. Crystallogr. 44 (2011) 1272–1276.

[49] F.G. Figueiras, I.K. Bdikin, V.B.S. Amaral, A.L. Kholkin, Local bias induced ferroelectricity in manganites with competing charge and orbital order states, Phys. Chem. Chem. Phys. 16 (2014) 4977–4981.

[50] J.P.B. Silva, K. Kamakshi, K.C. Sekhar, J.A. Moreira, A. Almeida, M. Pereira, M.J. M. Gomes, Ferroelectric polarization and resistive switching characteristics of ion beam assisted sputter deposited $BaTiO_3$ thin films, J. Phys. Chem. Solids 92 (2016) 7–10.

[51] S. Dutta, P. Buragohain, S. Glinsek, C. Richter, H. Aramberri, H. Lu, U. Schroeder, E. Defay, A. Gruverman, J. Íñiguez, Piezoelectricity in hafnia, Nat. Commun. 12 (2021) 7301.

[52] X. Li, C. Li, Z. Xu, Y. Li, Y. Yang, H. Hu, Z. Jiang, J. Wang, J. Ren, C. Zheng, C. Lu, Z. Wen, Ferroelectric properties and polarization fatigue of La:HfO$_2$ thin-film capacitors, Phys. Status Solidi RRL 15 (2021), 2000481.

[53] N.H. Fletcher, K.W. Lodge, J.W. Matthews, Epitaxial Growth, Part B, Academic Press, New York, 1975, p. 529.

[54] A. Trampert, K.H. Ploog, Heteroepitaxy of large-misfit systems: role of coincidence lattice, Cryst. Res. Technol. 35 (2000) 793–806.

[55] S. Estandía, N. Dix, M.F. Chisholm, I. Fina, F. Sánchez, Domain-matching epitaxy of ferroelectric Hf$_{0.5}$Zr$_{0.5}$O$_2$(111) on La$_{2/3}$Sr$_{1/3}$MnO$_3$(001), Cryst. Growth Des. 20 (2020) 3801–3806.

[56] T. Song, S. Estandía, H. Tan, N. Dix, J. Gàzquez, I. Fina, F. Sánchez, Positive effect of parasitic monoclinic phase of Hf$_{0.5}$Zr$_{0.5}$O$_2$ on ferroelectric endurance, Adv. Electron.Mater. 8 (2022), 2100420.

[57] H. Pan, S. Lan, S.X. Zhang, H. Yao, Y. Liu, F.M.J. Guo, L. Gu, D. Yi, X.R. Wang, H. Huang, J.L. Macmanus-Driscoll, L.Q. Chen, K.J. Jin, C.W. Nan, Y.H. Lin, Ultrahigh energy storage in superparaelectric relaxor ferroelectrics, Science 374 (2021) 100.

[58] I. Fina, F. Sánchez, Epitaxial ferroelectric HfO$_2$ films: growth, properties, and devices, ACS Appl. Electron. Mater. 3 (2021) 1530–1549.

[59] Y. Wei, G. Vats, B. Noheda, Synaptic behaviour in ferroelectric epitaxial rhombohedral Hf$_{0.5}$Zr$_{0.5}$O$_2$ thin films, Neuromorphol. Comput. Eng. (2022), https://doi.org/10.1088/2634-4386/ac970c press.

[60] https://www.psds.ac.uk/.

[61] R. Materlik, C. Künneth, A. Kersch, The origin of ferroelectricity in Hf$_{1-x}$Zr$_x$O$_2$: a computational investigation and a surface energy model, J. Appl. Phys. 117 (2015), 134109.

[62] S.S. Cheema, D. Kwon, N. Shanker, R. Reis, S.L. Hsu, J. Xiao, H. Zhang, R. Wagner, A. Datar, M.R. McCarter, C.R. Serrao, A.K. Yadav, G. Karbasian, C.H. Hsu, A.J. Tan, L.C. Wang, V. Thakare, X. Zhang, A. Mehta, E. Karapetrova, R.V. Chopdekar, P. Shafer, E. Arenholz, C. Hu, R. Proksch, R. Ramesh, J. Ciston, J.S. Salahuddin, Enhanced ferroelectricity in ultrathin films grown directly on silicon, Nature 580 (2020) 478–482.

[63] P. Nukala, Y. Wei, V. Haas, Q. Guo, J.A. Lleonart, B. Noheda, Guidelines for the stabilization of a polar rhombohedral phase in epitaxial Hf$_{0.5}$Zr$_{0.5}$O$_2$ thin films, Ferroelectrics 569 (2020) 148–163.

[64] R. Ganser, S. Bongarz, A.v. Mach, L.A. Antunes, A. Kersch, Piezo- and pyroelectricity in Zirconia: a study with machine learned force fields. https://arxiv.org/abs/2206.00540?context=cond-mat.